analytical chemistry

pubs.acs.org/ac Article

A Self-Powered Wearable Mechanoluminescent−Hydrovoltaic Patch for Multimodal Sensing Application and Energy Harvesting

Zhechen Zhang, Yuetong Tian, Shujia Wang, Zhida Gao, Yan-Yan Song,* Li-Ping Mei,* and Junjian Zhao*

Cite This: *Anal. Chem.* 2026, 98, 2098−2107 Read Online

ACCESS | Metrics & More | Article Recommendations | Supporting Information

ABSTRACT: Wearable electronics that enable multimodal sensing have the potential to revolutionize personalized health monitoring and human−machine interfaces. However, current sensors need to integrate several single-functional sensors to achieve multifunctional detection. Furthermore, the simultaneous generation, acquisition, and analysis of multimodal signals often result in high power consumption and may introduce electrical interference, thereby compromising the sensing accuracy. This study innovatively developed a self-powered mechanoluminescent (ML)−hydrovoltaic motion sensing patch for simultaneously monitoring human motion parameters and sweat electrolyte concentrations in one device without external energy input. Under various mechanical stimuli, parameters such as deformation frequency (0.33 Hz-1 Hz), intensity, direction, and sweat electrolyte levels can be directly inferred from the waveform and amplitude of the output voltage. Furthermore, secreted sweat serves as both a sensing medium and an energy source, driving continuous direct-current generation up to 0.584 V and 4.46 μA. A single sensing patch can achieve a maximum output power density of 7.9 mW/m^2 and demonstrate excellent durability for over 300 usage cycles. Based on this unique design strategy, the sensing patch is programmed and utilized for information transport, demonstrating its potential in human−machine interaction. This multidimensional, self-powered patch offers a platform for integrated motion sensing, biochemical monitoring, and energy harvesting in next-generation wearables.

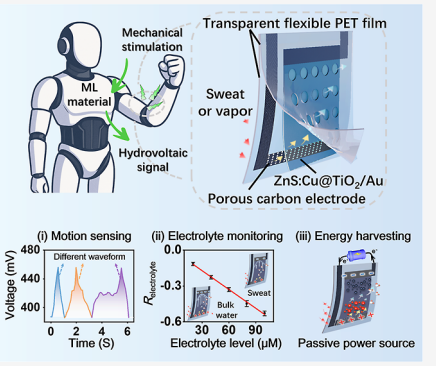

INTRODUCTION

Wearable electronics capable of simultaneous, real-time monitoring of multimodal physical and chemical signals such as human motion, electrolyte, and metabolite level have significant potential to advance personalized healthcare and human−machine interfaces.[1−5] To achieve multimodal sensing applications, current sensors need to integrate several single-functional sensors to achieve multifunctional detection. Furthermore, generating, recording, and analyzing these multimodal signals with the corresponding sensors can drain power and electrically interfere with the accuracy of sensor readings. Conventional motion sensors based on capacity variation,[6,7] resistance variation,[8−10] nanogenerators,[11−15] and other effects[16−18] are typically limited to a single sensing function. An "all-in-one" device that can simultaneously function without external energy input provides various physical parameters, and harvest energy is in urgent demand to solve the problem associated with long-term human−machine interaction. Hydrovoltaic-based sensors, used in drug detection,[19] chiral recognition,[20] and physical monitoring,[21,22] are considered as a promising next-generation self-powered sensing technology due to their advantages such as low cost, eco-friendliness, and ease of large-scale production. Interacting with the sensing medium allows the hydrovoltaic output voltage to directly reflect sensing results without requiring external energy input.[23,24] The hydrovoltaic effect enables the generation of electricity through interaction between nanostructured materials and water, addressing the energy consumption issue of wearable sensors. For hydrovoltaic-based sensors, the sensing information is directly encoded in the output voltage, eliminating the requirement for additional signal collection, processing, or transduction. Furthermore, the electricity generated by the hydrovoltaic-based sensors is direct current which can be directly harvested and utilized.[25−28] Despite these advantages, efficiently converting mechanical stimuli into hydrovoltaic signals remains unresolved, limiting practical motion-sensing applications. Thus, a strategy integrating hydrovoltaic sensing with mechanical energy harvesting is urgently required.

Integrating photoelectrochemical[29,30] and photocatalytic[31] system into hydrovoltaic device offers a promising route to

Received: September 8, 2025
Revised: January 6, 2026
Accepted: January 12, 2026
Published: January 14, 2026

https://doi.org/10.1021/acs.analchem.5c05546
Anal. Chem. 2026, 98, 2098−2107

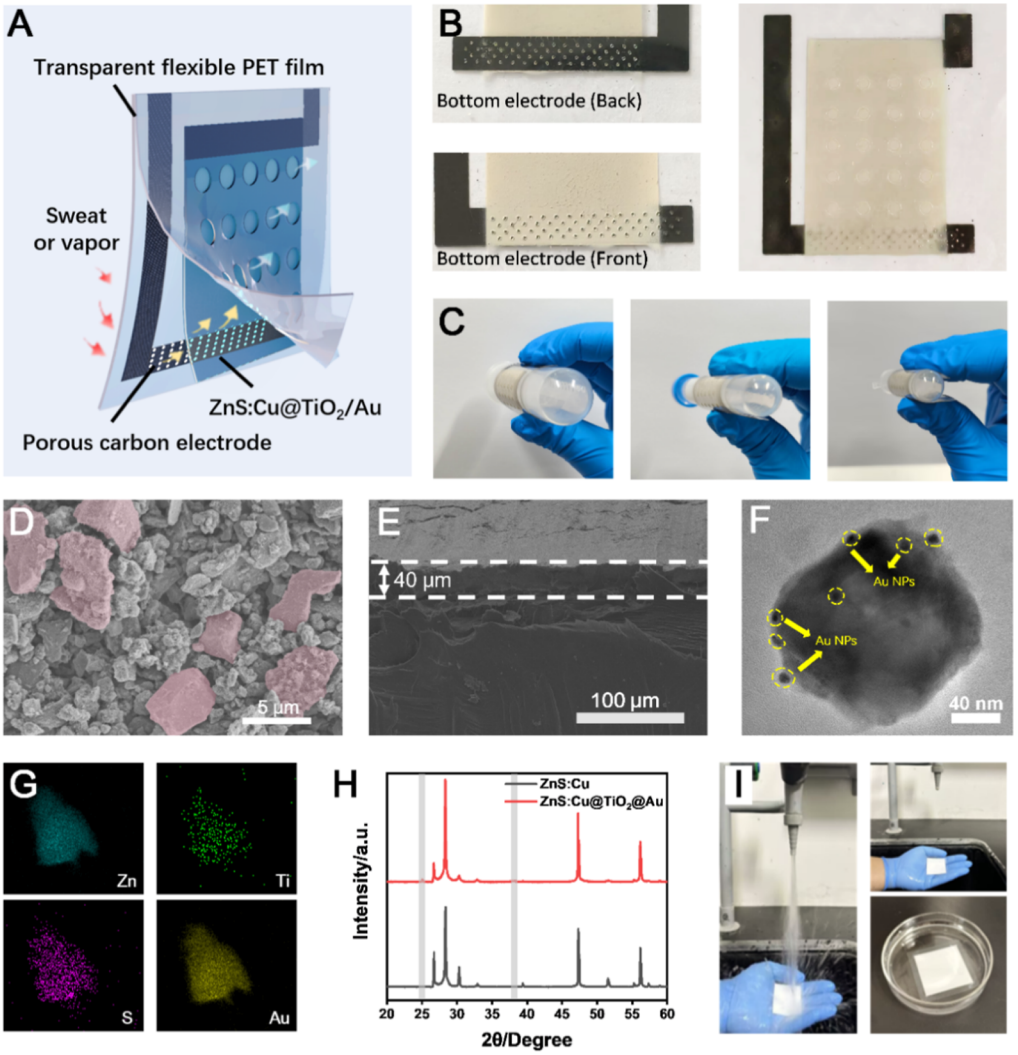

Figure 1. (A) Schematic illustration of design and composition of the hydrovoltaic sensing patch. (B) Optical images that exhibit the through-hole structure of the upper and bottom PET substrate. (C) Optical image that illustrates the flexibility of the motion sensing patch. Characterization of the ZnS:Cu@TiO_2/Au/PAN hydrovoltaic sensing layer. (D) Top view. (E) Side view. (F) TEM image. (G) EDS mapping images. (H) XRD patterns of ZnS:Cu@TiO_2/Au/PAN and commercial ZnS:Cu nanoparticles. (I) Optical images of the sensing patch without encapsulation film under/after water impact and after a long period of immersion.

modulate their output performance and broaden the potential application scenarios of hydrovoltaic-based sensors. By incorporating hydrogen generation and light energy conversion, moderate light stimulation can promote the generation, separation, and transmission of carriers within the hydrovoltaic device while also reestablishing the ion concentration gradient within the hydrovoltaic device. Mechanoluminescence (ML), which converts mechanical stimuli into visible or near-infrared emission,[32] offers excellent real-time response,[33] repeatability,[34] and reliable stress-luminescence properties.[35] ML materials are capable of capturing detailed motion parameters such as frequency, strength, and direction and transducing the captured motion signals into different luminescent responses. Variations in mechanical input directly influence both the duration and the intensity of the mechanoluminescent emission. The combination of an ML-based light source and hydrovoltaic effects thus provides a novel strategy for constructing multifunctional, self-powered motion sensors suitable for next-generation wearable electronics and human−machine interfaces.

In this study, we integrated mechanoluminescent material into a hydrovoltaic patch to achieve simultaneous motion sensing, electrolyte monitoring, and energy harvesting from human sweat without external energy input in a single device. By constructing the ZnS:Cu@TiO_2/Au interface to utilize the light emitted by the mechanoluminescent ZnS:Cu under mechanical stimuli, this flexible patch distinctly identifies human motion characteristics—including frequency (0.33 Hz−1 Hz), intensity, and direction—and transduces these signals directly into hydrovoltaic voltage outputs. Concurrently, the device accurately monitors sweat electrolyte concentrations with a limit of detection of 8.15 mM, enabling a real-time biochemical assessment. Furthermore, by leveraging the intrinsic hydrovoltaic effect, this sensing patch uniquely realizes continuous sweat-to-electricity conversion, generating stable direct current (DC) output without additional rectification components. A single sensing patch can generate an output voltage and current up to 0.584 V and 4.46 μA and a maximum output power density of 7.9 mW/m^2. Based on this unique design strategy, the intelligent motion sensing patch is programmed and utilized to transport messages via body

https://doi.org/10.1021/acs.analchem.5c05546
Anal. Chem. 2026, 98, 2098−2107

moment. This multifunctional, self-powered sensing strategy thus establishes a paradigm for integrated motion sensing, biochemical monitoring, and energy harvesting in wearable electronics and human−machine interaction applications.

EXPERIMENTAL SECTION

Preparation of Flexible PAN/ZnS:Cu@TiO_2/Au Mechanoluminescence Sensing Coating

An amorphous TiO_2 layer was coated onto commercial ZnS:Cu nanoparticles by using a wet-chemistry method. First, a ZnS:Cu nanoparticle suspension was prepared by dispersing 2 g of ZnS:Cu nanoparticles in 5 mL of ethanol under ultrasound for 10 min. This suspension was then mixed with 40 mL of ethanol, 0.2 mL of 28 wt % aqueous ammonia, and sonicated for 15 min, followed by stirring for 1 h. Next, 500 μL of tetrabutyl titanate was added into the reaction system, followed by stirring for 12 h at 45 °C. The resultant ZnS:Cu@TiO_2 NPs were collected by centrifugation at 10,000 rpm, washed three times with ethanol, and dried at 60 °C for 12 h. The resulted powder sample was annealed at 450 °C for 2 h in an Ar atmosphere to transform the crystalline structure to anatase. For the preparation of the ZnS:Cu@TiO_2/Au NPs, 1 g of ZnS:Cu@TiO_2 NPs was immersed in 50 mL of a 0.5 mM $HAuCl_4$ solution and stirred for 4 h. The pH value of the $HAuCl_4$ solution was adjusted to 7 by 0.1 M NaOH. Then, an LED UV light source was used to in situ photocatalytically reduce Au^{3+} to Au nanoparticles (AuNPs). The resulting samples were collected by centrifugation, washed with ethanol for 3 times, and vacuum dried for 12 h at 60 °C. The products were labeled as ZnS:Cu@TiO_2/Au NPs. To prepare the flexible tough PAN/ZnS:Cu@TiO_2/Au NP-active mechanoluminescence sensing coating, 0.3 g of PAN was first dissolved in 100 mL of DMF. Then, 6 g of ZnS:Cu@TiO_2/Au NPs was dispersed in the prepared solution by a 300 W sonication for 120 min to obtain the final PAN/ZnS:Cu@TiO_2/Au DMF coating.

Fabrication of the Self-Powered Motion-Sensing Patch

Thermoplastic PET sealing film with a thickness of 70 μm was used as the flexible substrate. Two L-shaped carbon electrodes were printed onto the flexible substrate by screen printing. The detailed design of the electrode is shown in Supporting Information. The as-printed electrode was dried at 50 °C overnight for further use. An array of through holes with diameters of 200 μm was constructed at the bottom L-shaped carbon electrode region on the PET film by using a CO_2-laser cutter. Both the carbon electrode was wired by the conductive copper tape. The lower electrode served as the positive electrode, while the upper electrode served as the negative electrode. The active mechanoluminescence hydrovoltaic sensing coating was sprayed into a specific 4 cm × 4 cm pattern using a masking plate, and the sensing film's thickness was controlled by adjusting the spraying duration. Following the sensing layer fabrication process, another thermoplastic PET film with an array of 2 mm through holes was used to encapsulate the sensing patch. A thermal laminator was used for packing the sensing patch at 80 °C.

RESULTS AND DISCUSSION

Design and Characterization of the Mechanoluminescence Hydrovoltaic Motion Sensing Patch

Figure 1A schematically illustrates the composition and structure of the flexible self-powered hydrovoltaic sensing patch. Mechanoluminescence ZnS:Cu@TiO_2/Au was employed as the hydro voltaic motion sensing material in the middle, sandwiched by two PET films coated with EVA layers at the top and bottom for encapsulating. The thermoplastic ethylene−vinyl acetate copolymer (EVA) coated on the PET substrate is applied to bond the mechanoluminescence hydrovoltaic sensing layer after heat sealing. The bottom PET substrate coated with conductive carbon paint serves as the bottom electrode for the self-powered sensing patch, as well as the adhesive layer and spacer for in situ sweat sampling and transporting. Induced by evaporation, the sweat or vapor secreted from the body surface will be collected and transported to the ZnS:Cu@TiO_2/Au mechanoluminescence hydrovoltaic active sensing coating through the bottom porous PET film, resulting in the sensing signal and output voltage. The detailed design of the sensing patch is shown in Figure S1. The conductive carbon electrode was printed onto the bottom flexible PET substrate by screen-printing (details are shown in Figure S2). A through-hole array with a diameter of 200 μm was fabricated onto the bottom electrode with a CO_2 laser cutter (Figure 1B). The PAN/ZnS:Cu@TiO_2/Au mechanoluminescence hydrovoltaic active sensing coating was sprayed onto the bottom PET substrate. The top layer consists of a PET substrate featuring a 5 × 4 array of through-holes, each with a diameter of 2 mm (Figure 1B). The incorporation of EVA and PAN significantly enhances the mechanical robustness of the sensing layer, allowing the final patch to tolerate mechanical deformation, such as bending with various radii (Figures 1C and S3).

Under mechanical stimulation, ZnS:Cu typically emits visible light in the range of 450−600 nm. Consequently, a ZnS:Cu@TiO_2/Au interface is constructed to effectively harness the emitted light. The ZnS:Cu@TiO_2/Au NPs are synthesized by a typical wet-chemistry, followed by a photoreduction process. After the hydrolysis process, a layer of amorphous TiO_2 NPs is coated onto the ZnS:Cu NPs. Then, an annealing process was carried out to convert the amorphous TiO_2 into the anatase crystalline phase. AuNPs are modified onto the ZnS:Cu@TiO_2 NPs through a straightforward in situ photocatalytic reduction method. The resulting sample is defined as ZnS:Cu@TiO_2/Au NPs. The morphology of the as-synthesized mechanoluminescence hydrovoltaic active sensing layer is characterized by scanning electron microscopy (SEM) as presented in Figures 1D and S4, revealing nanoparticle diameters ranging from 400 nm to 5 μm. Nanopores are formed by random stacking and interconnection of these nanoparticles. Cross-sectional SEM image shows particles tightly bound into a 40 μm-thick layer (Figure 1E). The TEM images reveal that the AuNPs are uniformly distributed over the surface of the TiO_2 shell, which is coated on the ZnS:Cu (Figures 1F and S5). EDS mapping of Zn, Ti, S, and Au elements confirms the uniform distribution of AuNPs, TiO_2, and the bonding agent PAN (Figure 1G). Fourier transform infrared spectra (FT-IR) of the PAN/ZnS:Cu@TiO_2/Au active sensing layer shows the vibration absorption bands of −C≡N groups from PAN at 2245 cm^{-1}, verifying the successful loading of PAN (Figure S6). Figures 1H and S7 show the XRD patterns of the as-prepared active sensing coating. The characteristic diffraction peaks of the ZnS:Cu@TiO_2@Au active sensing layer at 25.3°and 38.2° demonstrate the successful decoration of the AuNPs and TiO_2 shell on the ZnS:Cu core without altering the crystal structure of ZnS:Cu. The Zeta potential of the sensing film during various modification processes is tested. As shown in Figure S8, due to the strong polarity of the cyanide-containing PAN, the PAN modification process does not affect the surface charge density of the sensing film. After the AuNP modification process, a significant absorption peak is observed in the visible-light spectrum (400−700 nm), which is attributed to the optical absorption of scattered light by the

https://doi.org/10.1021/acs.analchem.5c05546
Anal. Chem. 2026, 98, 2098−2107

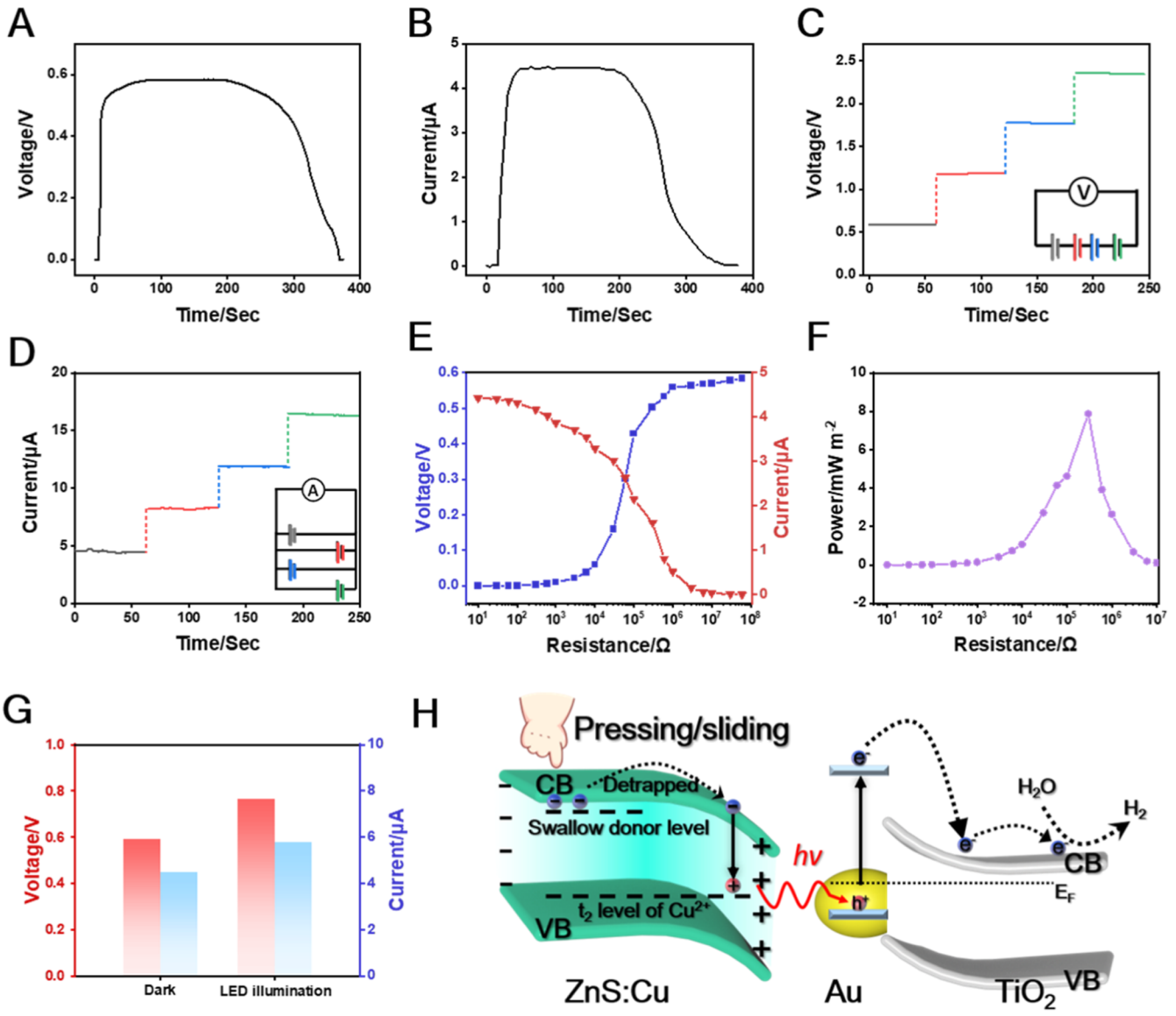

Figure 2. (A) Output voltage−time curve of a single sensing patch. (B) Output current−time curve of a single sensing patch. (C) Output voltage of the sensing patch arrays connected in series. (D) Output current of the sensing patch arrays connected in parallel. (E) Output voltage and current of a single sensing patch under various load resistances. (F) Output power performance of the sensing patch under various load resistances. (G) Output voltage and current of the sensing patch with and without LED illumination. (H) Schematic diagram illustrating the mechanism of mechanical-to-hydrovoltaic energy conversion.

LSPR effect of AuNPs (Figure S9). The introduction of AuNPs effectively enhances the collection and utilization of light emitted by mechanoluminescent ZnS:Cu. To further investigate the stability of the as-prepared sensing coating, a water-impacting and immersion experiment is carried out. The mechanoluminescence hydrovoltaic sensing patch, without its upper sealing, is put under a water drain, with the water flow impacting the surface of the sensing coating. The sensing film maintained its structural integrity. Prolonged immersion in deionized (DI) water also do not cause any damage to the sensing film (Figure 1I).

Output Performance Evaluation of the Mechanoluminescence Hydrovoltaic Motion Sensing Patch

Based on the hydrovoltaic effect, when the sensing coating interacts with the sweat or vapor secreted from the body surface, the charged nanochannel within the sensing film will promote the counterions to move along the evaporation direction while preventing the like-charged ions. Thus, a stable potential difference will be generated between the upper and the bottom electrodes, donating the hydrovoltaic voltage. To evaluate the output performance of the sensing patch, the output voltage and current of a sensing patch with a working area of 4 × 4 cm is measured. The sensing patch is driven by 1.5 μL of DI water. A small amount of water enabled the sensing patch to produce a stable hydrovoltaic output voltage for over 300 s. The volume of water used to drive the sensing patch only affects the output current (Figure S10). When the sensing patch interacts with the water, the output voltage rapidly reaches 0.584 V in ∼68 s (Figure 2A). Concurrently, the output current also increased to 4.46 μA (Figure 2B). Utilizing the simple fabrication process, the sensing patch can be integrated into a patch array. By connecting the patches in series or parallel, the output performance can be significantly

https://doi.org/10.1021/acs.analchem.5c05546
Anal. Chem. 2026, 98, 2098−2107

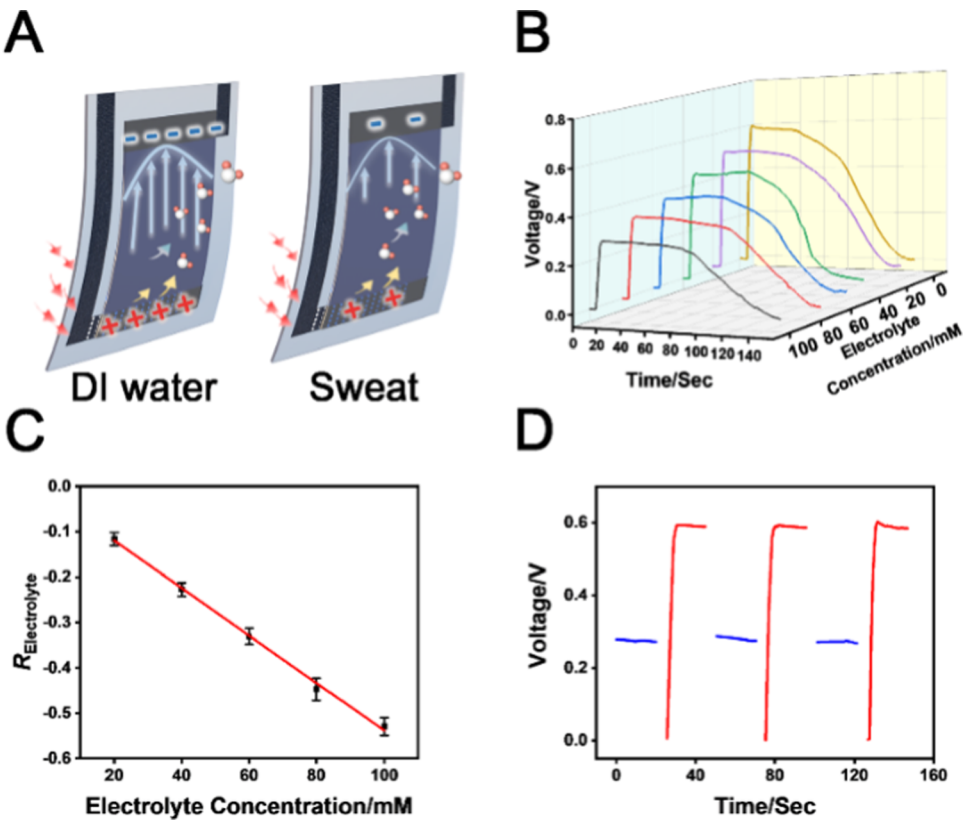

Figure 3. (A) Schematic depiction of the working mechanism of real-time electrolyte monitoring by the hydrovoltaic sensing patch. (B) Output voltage−time curve of a single sensing patch under various NaCl concentrations. (C) Calibration curve of the sensor response as a function of the NaCl concentration. (D) Output performance changes of the hydrovoltaic motion sensing patch in 100 mM NaCl solution and after the immersion process in DI water.

enhanced. As illustrated in Figure 2C and D, the output voltage and current linearly increase to 2.35 V and 16.4 μA, respectively, when four sensing patches are connected or parallel. The output performance of a single sensing patch is evaluated using various load resistances. As the load resistance increases, the open-circuit voltage rises, whereas the output current decreases (Figure 2E). The maximum output power density is achieved at 7.9 mW m^{-2} with a load resistance of 3×10^6 Ω (Figure 2F). The output voltage and current of the as-prepared sensing patch under LED illumination are investigated. The spectrum of the LED light is shown in Figure S11.

Under LED illumination, the output voltage and current of the sensing patch show a significant increase which is due to the LSPR effect of AuNPs (Figure 2G). The output voltage of the device increases with increasing light intensity (Figure S12), which exhibits the potential of reflecting the mechanical stimulation by the output voltage by using mechanoluminescent materials. The output performance of the sensing patch was also evaluated under simulated sunlight, demonstrating its potential for outdoor applications (Figure S13). When replacing the light stimulation with force stimulation to the mechanoluminescent ZnS:Cu, the mechanism of hydrovoltaic voltage increase is shown in Figure 2H. Piezoelectric polarization charges are generated within piezoelectric ZnS under either pressing or sliding stimulation, attributed to its noncentral symmetry.[36,37] The piezo-charge-induced piezo potential effectively tilts the band structure, facilitating the detrapping of electrons into the conduction band of ZnS:Cu nanoparticles.[38] Inevitably, recombination between the detrapped electrons and holes occurs, releasing energy that excites the dopant Cu^{2+} ions instead of emitting a photon. When the excited Cu^{2+} ion returns to its ground state, it emits a photon in the form of green visible light. The emitted light is absorbed by AuNPs due to the surface plasmon resonance effect. High-energy hot electrons in plasmonic Au are transiently generated and then injected into the CB of TiO_2 for photocatalysis reaction. This photocatalysis reaction consumed the hydrogen ions and disrupted the original counterion equilibrium, leading to a higher streaming potential.

Electrolyte Sensing Performance of the Sensing Patch

Electrolyte in sweat contains useful indicators that help monitor human health status. Based on the Debye−Hückel equation, the debye length (λ_D), which is a reflection of shielding ability of charged nanochannel, decreases as ion concentration increases. When the electrolyte concentration in secreted sweat increases, the electrical double layer (EDL) within the nanochannel becomes compressed. Consequently, as water flows upward, fewer hydroxide ions reach the top of the sensing patch, resulting in a lower output voltage from the sensing patch (Figure 3A). Figure 3B displays the output voltage−time curve of the sensing patch across varying electrolyte concentrations from 0 to 100 mM. The NaCl solution is used as the model electrolyte. The electrolyte response ($R_{electrolyte}$) is calculated as below:

$$R_{electrolyte} = (V_{electrolyte} - V_0)/V_0 \quad (1)$$

where V_0 and $V_{electrolyte}$ represent the output voltage of the sensing patch before and after electrolyte sensing, respectively.

https://doi.org/10.1021/acs.analchem.5c05546
Anal. Chem. 2026, 98, 2098−2107

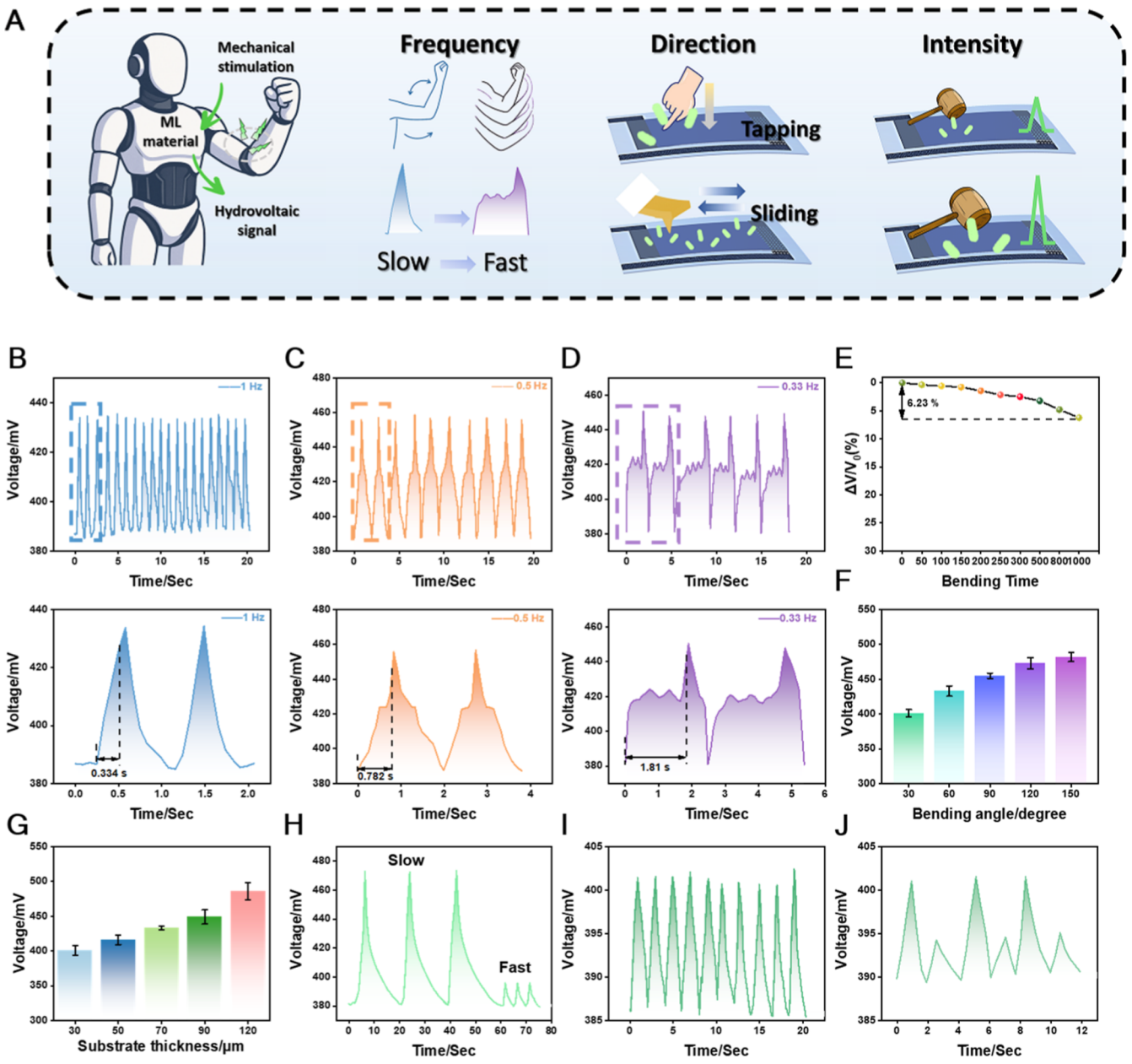

Figure 4. (A) Scheme of simultaneous monitoring motion frequency, direction, and intensity by the ML−hydrovoltaic motion sensing patch. (B−D) The bending response output performance of the hydrovoltaic motion sensing patch under various bending frequencies of 1, 0.5, and 0.33 Hz is tested, respectively. The real-time output voltage−time curves of the previous two bending processes are shown below, respectively. (E) The sensing output performance loss of the sensing patch after different bending times. (F) The sensing output performance of the sensing patch under different bending angles. (G) The sensing output performance of the sensing patch using various thicknesses of the encapsulating film. (H) The sliding sensing output performance of the sensing patch under continuously reciprocating sliding stimulations with different sliding speeds. (I) The knocking sensing performance of the sensing patch that was continuously knocked using a 100 g metal tip. (J) The knocking sensing performance of the sensing patch that was continuously knocked by two tips of different weights, alternately.

The response value shows a linear relationship with the electrolyte concentration (Figure 3C). The limit of detection of the sensing patch is 8.15 mM based on a 3SD/L method. Real sweat was also tested to further assess the reliability of the sensing patch (Figure S14). The total electrolyte concentration measured by the device was 59.3 mM. To further investigate the reliability of the sensing patch, the sensing patch used is washed with DI water to remove the accumulated ions. As shown in Figure 3D, the rinse process does not affect the electrolyte sensing performance, indicating the excellent reliability of the sensing patch.

Motion Sensing Performance of the Self-Powered Sensing Patch

Aiming at long-term motion sensing ability, the stability and repeatability of light emitting performance of the sensing patch are carefully investigated and presented. Under either pressing or sliding stimulation, the green-light-emitting irradiation is triggered. The emitting spectrum of the as-prepared motion sensing patch is shown in Figure S15. Generally, these motion sensing patches exhibit a stable ML intensity throughout the whole test during a continuous sliding stimulation triggered by a linear module equipped with a metal tip (Figure S16). The

https://doi.org/10.1021/acs.analchem.5c05546
Anal. Chem. 2026, 98, 2098−2107

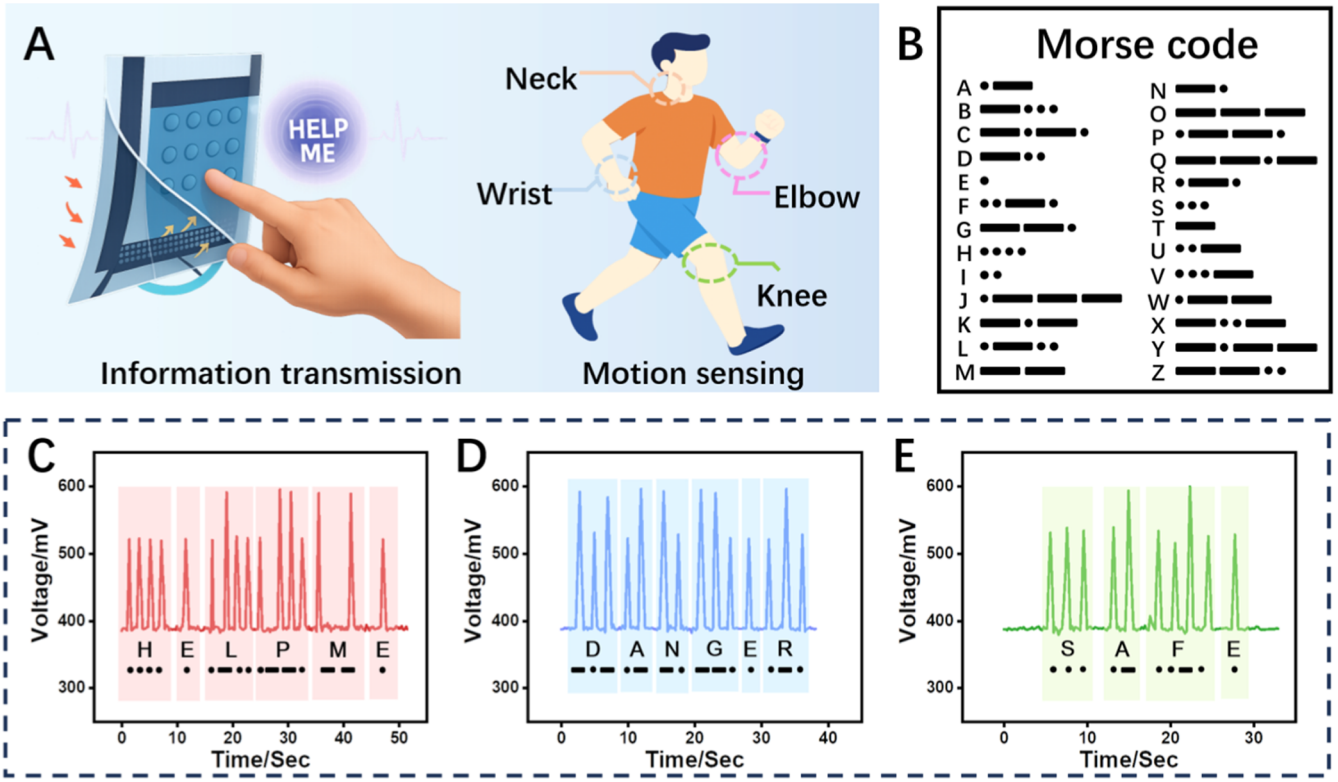

Figure 5. (A) Schematic diagram of the application of the motion sensing patch. Morse code transmission. (B) The international Morse code. (C) The message relates to "HEPLME". (D) The message relates to "DANGER". (E) The message relates to "SAFE".

flexibility and mechanical robustness of the sensing patch are studied by a cyclical bending test, in which the sensing patch is attached to customized fixtures moving back and forth, as shown in Figure S17. As shown in Figure S18, the sensing patch exhibits a stable emitting performance, while the light-emitting intensity under bending stimulation is lower than the luminescent intensity during sliding.

Utilizing the innovative design of combining the ML materials with hydrovoltaic sensors, the as-prepared motion sensing patch can achieve discrimination of various motion frequencies, directions, and intensities (Figure 4A). Considering that when a motion sensor is utilized in a practical scenario, the frequency and magnitude of the mechanical pressure applied to the sensing patch are irregular, so it is necessary to analyze the sensor performance of sensing patch under different circumstances. The electrical output of the sensing patch was quantified under different external mechanical stimulation. Stimulations of various frequencies, bending radii, as well as directions are simulated by a reciprocating robot arm, while strengths are simulated by different weights. The sensing patch is driven by 80 mM NaCl solution in this section. Figure 4B−D illustrates the output voltage−time curve of the sensing patch with a bending frequency of 1, 0.5, and 0.33 Hz, respectively. The bending angle is controlled as 60°. The various bending frequency does not affect the peak voltage of the sensing patch. However, the waveform of the output voltage is quite different. When the bending frequency is set as 1 Hz, the output voltage directly reaches to the maximum values and then decays to the baseline, while the output voltage will first come to a stable value when the bending frequency is 0.5 and 0.33 Hz. During one operating cycle, the time that the maximum voltage occurs varies with bending frequency. To further characterize the sensitivity of the sensing patch, the response time, which is defined as the time cost by the sensing patch to reach 90% of the maximum output voltage, is investigated. Due to the increase of bending frequency, the working time of each cycle is shortened, and the response time is increased accordingly from 0.334 s at the initial 1 Hz to 1.81 s at 0.33 Hz. The recovery time which was defined as the time taken to acquire 90% variation in the sensor output performance was also investigated. The recovery time for 1, 0.5, and 3 Hz was 0.383, 1.002, and 0.521 s, respectively (Figure S19). The as-prepared sensing patch shows only little output performance degradation at over 1000 cycles, indicating the excellent stability and long-term robustness of the sensing performance (Figure 4E). The sensing performance of the sensing patch with different bending angles is also tested. By shortening the telescoping distance of the reciprocating arm, bending simulation of various bending angles can be achieved. During the bending angle test, the bending frequency is set at 1 Hz. As shown in Figure 4F, as the bending angle increases, an enhancement of the output voltage is found. This is because of the stronger stress that will be applied to the mechanoluminescent ZnS:Cu with the larger bending angle. Noted that excessive bending angles will cause plastic deformation of the thermoplastic film, which will affect the repeatability of the sensing performance. By alteration of the thickness of the encapsulating film, the sensing response of the as-prepared patch under bending stimulation can be effectively modified (Figure 4G). A thicker PET sealing film will provide a better sensing performance. However, an over thick sealing film will affect the flexibility of the device. When the sensing patch is attached to the joint part of the body, it is inevitable for the sensing patch to withstand the forces not only from the bending direction but also from the vertical direction. The vertical force applied to the sensing patch is simulated by a

https://doi.org/10.1021/acs.analchem.5c05546
Anal. Chem. 2026, 98, 2098−2107

linear module equipped with a metal tip. A sliding and knocking process is carried out onto the surface of the sensing patch to simulate different kinds of vertical force. As shown in Figure 4H, continuous reciprocating sliding stimulations with different sliding speeds are carried out. The reciprocating distance is 4 cm, corresponding to the length of the active sensing coating. The slower sliding will lead to a long-last luminescent process, resulting in a higher output voltage. The peak voltage of each sliding process exhibits excellent repeatability. A continuous knocking stimulation with a working frequency of 0.5 Hz is utilized to investigate the sensing performance of the patch to prompt impact. The weight of the metal tip is 100 g, and the contact area between the sensing patch and the tip is 0.125 cm^2. When the metal tip quickly hits the surface of the sensing patch, the output voltage rapidly increases to 401 mV in a response time of 0.71 s (Figure 4I). To investigate the relationship between the sensing output voltage and the knocking strength, the sensing patch is continuously knocked by a 100 g metal tip and a 50 g one. Both tips have the same contact area. As shown in Figure 4J, when the sensing patch was knocked by two tips alternately, the sensing output voltage corresponding to the various tips occurs, respectively. This phenomenon indicates that the prepared sensing patch exhibits a superior sensitivity.

Application of the Motion Sensing Patch

The successful combination of ML materials with hydrovoltaic sensing chips enables continuous self-powered sensing in one device, offering a simplified alternative with significant potential in healthcare, motion monitoring, and information transmission. The wearable sensing patch was further programmed and utilized for Morse code transmission, as illustrated in Figure 5A. The sensing patch was attached to the joint area of the arm. Prior to the test, the volunteers exercised for 30 min to induce continuous perspiration. The volunteer's physical movements were programmed to represent Morse code. The Morse code transmission was achieved by encoding arm bending as "dot", while finger tapping was programmed as "dash" and both types of motion stimuli are applied at a frequency of 1 Hz, in accordance with international Morse code standards (Figure 5B). When the sensing patch was activated by different motion stimuli, massages as "HELPME", "DANGER", and "SAFE" were successfully transmitted via the Morse code (Figure 5C−E). This capacity of information transmission highlights the potential of the as-prepared ML−hydrovoltaic sensing patch for real-time communication in emergency situations.

CONCLUSION

In this work, we integrated mechanoluminescent ZnS:Cu@TiO_2/Au nanoparticles within a charged nanochannel hydrovoltaic film to achieve simultaneous multifunctional sensing applications and energy harvesting. The design of the combination of ML material with hydrovoltaic sensing chips realizes the simultaneous discrimination and monitoring of human motions and sweat electrolyte level in a single device without external energy input. By analyzing the waveform and amplitude of the output hydrovoltaic voltage, parameters such as deformation frequency (0.33 Hz−1 Hz), intensity, direction, and sweat electrolyte levels can be directly read out. Furthermore, a 4 cm × 4 cm sensing patch enables a continuous sweat-to-electricity process that can deliver up to 0.584 V and 4.46 μA. Based on this unique design strategy, the flexible self-powered motion sensing patch is programmed to send a message via body movement. This multidimensional, self-powered patch offers a platform for integrated motion sensing, biochemical monitoring, and energy harvesting in next-generation wearables, demonstrating its great potential in human−machine interaction.

ASSOCIATED CONTENT

Supporting Information

The Supporting Information is available free of charge at https://pubs.acs.org/doi/10.1021/acs.analchem.5c05546.

Experimental Details, characterizations, design of the sensing patch, SEM and TEM images of the ZnS:Cu@TiO_2/Au/PAN, FTIR and UV−vis spectrum of the active sensing layer, zeta potential of the sensing film, detail about the LED light source, emission spectrum of the sensing patch, and stability of the motion sensing patch (PDF)

AUTHOR INFORMATION

Corresponding Authors

Yan-Yan Song − *College of Sciences, Northeastern University, Shenyang 110819, P. R. China*; orcid.org/0000-0001-5150-4784; Email: yysong@mail.neu.edu.cn

Li-Ping Mei − *College of Geography and Environmental Sciences, Zhejiang Normal University, Jinhua 321004, China*; orcid.org/0000-0002-5067-3006; Email: mei.lp@zjnu.edu.cn

Junjian Zhao − *Department of Pharmacy, Shenyang Medical College, Shenyang 110034, P. R. China*; Email: jjzhao@symc.edu.cn

Authors

Zhechen Zhang − *College of Sciences, Northeastern University, Shenyang 110819, P. R. China*

Yuetong Tian − *College of Sciences, Northeastern University, Shenyang 110819, P. R. China*

Shujia Wang − *College of Sciences, Northeastern University, Shenyang 110819, P. R. China*

Zhida Gao − *College of Sciences, Northeastern University, Shenyang 110819, P. R. China*; orcid.org/0000-0002-9804-8170

Complete contact information is available at: https://pubs.acs.org/10.1021/acs.analchem.5c05546

Author Contributions

The manuscript was written through contributions of all authors. All authors have given approval to the final version of the manuscript.

Funding

This work was supported by the National Natural Science Foundation of China, China (No. 22374015); Liaoning Province Foundation for Distinguished Young Scholars, China (No. 1727146584490, to Y.-Y.S.); Fundamental Research Funds for the Central Universities, China (N25QNR014); and the PhD Start-up Foundation of Liaoning Province, China (No. 2025-BS-0868).

Notes

The authors declare no competing financial interest.

■ ACKNOWLEDGMENTS

Special thanks are due to the instrumental or data analysis from the Analytical and Testing Center, Northeastern University.

■ REFERENCES

(1) Ma, C. B.; Shang, X. D.; Sun, M. M.; Bo, X.; Bai, J.; Du, Y.; Zhou, M. Emerging Multifunctional Wearable Sensors: Integrating Multimodal Sweat Analysis and Advanced Material Technologies for Next-Generation Health Monitoring. *ACS Sens.* **2025**, *10* (4), 2388−2408.

(2) Li, C.; Hu, J.; Gao, G.; Chen, J.; Wang, C.; Zhou, H.; Chen, G. X.; Qu, P.; Lin, P.; Zhao, W. W. Biomolecules-Incorporated Metal-Organic Frameworks Gated Light-Sensitive Organic Photoelectrochemical Transistor for Biodetection. *Adv. Funct. Mater.* **2022**, *33*, 2211277.

(3) Chen, Z. F.; Fu, X. X.; Yu, J. X.; Qiu, H. Y.; Ren, S. B.; Wang, C. Y.; Han, M. D.; Zhao, W. W. Biological Transformation of AgI on MOF-on-MOF-Derived Heterostructures: Toward Polarity-Switchable Photoelectrochemical Biosensors for Neuron-Specific Enolase. *Anal. Chem.* **2023**, *95* (23), 9052−9059.

(4) Cai, J.; Deng, W.; Zhu, Z. Y.; Zheng, L.; Sun, M.; Ma, C. B.; Bai, J.; Bo, X.; Zhou, M. A Single Carbon Microyarn-Based Integrated Wearable Textile Sweat Sensor Built into a Hook-and-Loop Fastener. *Anal. Chem.* **2025**, *97* (29), 15771−15779.

(5) Zhang, Q.; Zhang, L.; Liu, N. X.; Li, J. Z.; Li, Z.; Wu, M. X.; Wang, L. G.; Zhao, W. W. Establishing Interfacial Charge-Transfer Transitions on Ferroelectric Perovskites: An Efficient Route for Photoelectrochemical Bioanalysis. *ACS Sens.* **2020**, *5* (12), 3827−3832.

(6) Sarwar, M. S.; Dobashi, Y.; Preston, C.; Wyss, J.; Mirabbasi, S.; Madden, J. D. W. Bend, Stretch, and Touch: Locating a Finger on an Actively Deformed Transparent Sensor Array. *Sci. Adv.* **2017**, *3*, No. e1602200.

(7) Wang, X.; Niu, H.; Gao, S.; Shen, G.; Li, Y. Bat-Inspired Bionic Bimodal Active Cognitive Electronic Skin with Multisensory Integration Ability. *Nano Lett.* **2025**, *25*, 5784−5793.

(8) Park, M.; Park, Y. J.; Chen, X.; Park, Y. K.; Kim, M. S.; Ahn, J. MoS_2-Based Tactile Sensor for Electronic Skin Applications. *Adv. Mater.* **2016**, *28*, 2556−2562.

(9) Zhuo, F.; Ding, Z.; Yang, X.; Chu, F.; Liu, Y.; Gao, Z.; Jin, H.; Dong, S.; Wang, X.; Luo, J. Advanced Morphological and Material Engineering for High-Performance Interfacial Iontronic Pressure Sensors. *Adv. Sci.* **2025**, *12*, 2413141.

(10) Cheng, K.; Zou, L.; Chang, B.; Liu, X.; Shi, H.; Li, T.; Yang, Q.; Guo, Z.; Liu, C.; Shen, C. Mechanically Robust and Conductive Poly(acrylamide) Nanocomposite Hydrogel by the Synergistic Effect of Vinyl Hybrid Silica Nanoparticle and Polypyrrole for Human Motion Sensing. *Adv. Compos. Hybrid Mater.* **2022**, *5*, 2834−2846.

(11) Lu, W.; Xu, Y.; Zou, Y.; Zhang, L.; Zhang, J.; Wu, W.; Song, G. Corrosion-Resistant and High-Performance Crumpled-Platinum-Based Triboelectric Nanogenerator for Self-Powered Motion Sensing. *Nano Energy* **2020**, *69*, 104430.

(12) Li, C.; Wang, P.; Zhang, D. Self-Healable, Stretchable Triboelectric Nanogenerators Based on Flexible Polyimide for Energy Harvesting and Self-Powered Sensors. *Nano Energy* **2023**, *109*, 108285.

(13) Shen, C.; Jia, L.; Yang, Y. Fully Medical Waste-Based Triboelectric Nanogenerator for Energy Harvesting and Intelligent Human Motion Sensing. *ACS Sustainable Chem. Eng.* **2024**, *12*, 14141−14152.

(14) Wei, C.; Cheng, R.; Ning, C.; Wei, X.; Peng, X.; Lv, T.; Sheng, F.; Dong, K.; Wang, Z. L. A Self-Powered Body Motion Sensing Network Integrated with Multiple Triboelectric Fabrics for Biometric Gait Recognition and Auxiliary Rehabilitation Training. *Adv. Funct. Mater.* **2023**, *33*, 2303562.

(15) So, M. Y.; Xu, B. Adaptive Ultra-Low Resilience Woven Triboelectric Nanogenerators for High-Performance Wearable Energy Harvesting and Motion Sensing. *Small* **2025**, *21*, 2501116.

(16) Wang, Q.; Jian, M.; Wang, C.; Zhang, Y. Carbonized Silk Nanofiber Membrane for Transparent and Sensitive Electronic Skin. *Adv. Funct. Mater.* **2017**, *27*, 1605657.

(17) Sun, Q.; Seung, W.; Kim, B. J.; Seo, S.; Kim, S. W.; Cho, J. H. Active Matrix Electronic Skin Strain Sensor Based on Piezopotential-Powered Graphene Transistors. *Adv. Mater.* **2015**, *27*, 3411−3417.

(18) Khan, U.; Kim, T. H.; Ryu, H.; Seung, W.; Kim, S. W. Graphene Tribotronics for Electronic Skin and Touch Screen Applications. *Adv. Mater.* **2017**, *29*, 1603544.

(19) Ding, H.; Jiang, D.; Du, X.; Zhang, Z.; Jiang, J.; Shan, X.; Wang, W.; Shiigi, H.; Chen, Z. Hydrovoltaic Effect Coupling with Capacitor Amplification: A Mode for Sensitive Self-Powered Electrochemical Sensing. *Anal. Chem.* **2023**, *95*, 12595−12599.

(20) Zhang, Z.; He, H.; Guo, J.; Zhao, C.; Gao, Z.; Song, Y. Y. Water Evaporation-Driven Arginine Enantiomer Recognition on a Self-Powered Flexible Chip with High Specificity. *Anal. Chem.* **2023**, *95*, 8128−8136.

(21) Huangfu, X.; Guo, Y.; Mugo, S. M.; Zhang, Q. Hydrovoltaic Nanogenerators for Self-Powered Sweat Electrolyte Analysis. *Small* **2023**, *19*, 2207134.

(22) Li, L.; Zheng, Z.; Ge, C.; Wang, Y.; Dai, H.; Li, L.; Wang, S.; Gao, Q.; Liu, M.; Sun, F.; Zhang, T. A Flexible Tough Hydrovoltaic Coating for Wearable Sensing Electronics. *Adv. Mater.* **2023**, *35*, 2304099.

(23) Shi, X.; Wei, Y.; Tang, B.; Li, Y.; Lv, L.; Lin, S.; Luo, S.; Wang, T.; Tan, S.; Sun, Q.; Wang, X.; Zheng, X.; Guo, Y.; Liang, F.; Huang, W.; Yu, H. D. A Kirigami-Driven Stretchable Paper-Based Hydrovoltaic Electricity Generator. *Adv. Funct. Mater.* **2025**, *35*, 2419753.

(24) Hu, Q.; Hong, M.; Wang, Z.; Lin, X.; Wang, W.; Zheng, W.; Zhou, S. Microbial Biofilm-Based Hydrovoltaic Pressure Sensor with Ultrahigh Sensitivity for Self-Powered Flexible Electronics. *Biosens. Bioelectron.* **2025**, *275*, 117220.

(25) Wang, Y.; Yuan, X.; Ni, K.; Song, Y.; Li, X.; Zeng, X.; Shao, B.; Sun, B. 3D Dendritic Hierarchically Gradient Nanoflowers in Situ Grown on Conductive Substrates for Efficient Hydrovoltaic Power Generation. *Energy Environ. Sci.* **2024**, *17*, 4780−4793.

(26) Shao, B.; Song, Z.; Chen, X.; Wu, Y.; Li, Y.; Song, C.; Yang, F.; Song, T.; Wang, Y.; Lee, S. T.; Sun, B. Bioinspired Hierarchical Nanofabric Electrode for Silicon Hydrovoltaic Device with Record Power Output. *ACS Nano* **2021**, *15*, 7472−7481.

(27) Li, J.; Wang, R.; Wang, C.; Xu, Y.; Cheng, W.; Wang, J.; Zhao, G.; Du, X.; Yang, H.; Ma, G.; Xu, Y.; Ye, Y.; Li, L.; Sun, Y.; Zhao, J.; Tang, R.; Zou, G. Three-Dimensional Synergistic Strategy for Enhancing Voltage Output of ZnO Hydrovoltaic Devices. *Adv. Funct. Mater.* **2025**, *35*, 2421130.

(28) Lin, J.; Zhang, Z.; Lin, X.; Cai, X.; Fu, S.; Fang, X.; Ding, Y.; Wang, X.; Sèbe, G.; Zhou, G. All Wood-Based Water Evaporation-Induced Electricity Generator. *Adv. Funct. Mater.* **2024**, *34*, 2314231.

(29) Zhang, Z.; Guo, J.; Zhao, J.; Tian, Y.; Gao, Z.; Song, P.; Song, Y. Y. Integrating Photoelectrochemical Feature on a Hydrovoltaic Chip with High-Salinity Adaption as a Self-Powered Device for Formaldehyde Monitoring. *ACS Sens.* **2024**, *9* (5), 2520−2528.

(30) Wang, C.; Hou, L.; Liu, S.; Kong, F.; Zhu, Y.; Wang, W.; Zhao, W. W. Simultaneously Realizing Signal-Switchability and Ultrahigh-Gain in a Graphene Photoelectrochemical Transistor Toward High-Performance Biological Detection. *Adv. Funct. Mater.* **2025**, No. e27361.

(31) Duan, P.; Wang, C.; Huang, Y.; Fu, C.; Lu, X.; Zhang, Y.; Yao, Y.; Chen, L.; He, Q. C.; Qian, L.; Yang, T. Moisture-based green energy harvesting over 600 hours via photocatalysis-enhanced hydrovoltaic effect. *Nat. Commun.* **2025**, *16*, 239.

(32) Zhuang, Y.; Xie, R. J. Mechanoluminescence Rebrightening the Prospects of Stress Sensing: A Review. *Adv. Mater.* **2021**, *33*, 2005925.

(33) Wang, C.; Yu, Y.; Yuan, Y.; Ren, C.; Liao, Q.; Wang, J.; Chai, Z.; Li, Q.; Li, Z. Heartbeat-Sensing Mechanoluminescent Device Based on a Quantitative Relationship between Pressure and Emissive Intensity. *Matter* **2020**, *2*, 181−193.

(34) Zeng, S.; Zhang, D.; Huang, W.; Wang, Z.; Freire, S. G.; Yu, X.; Smith, A. T.; Huang, E. Y.; Nguon, H.; Sun, L. Bio-Inspired Sensitive

https://doi.org/10.1021/acs.analchem.5c05546
Anal. Chem. 2026, 98, 2098−2107

and Reversible Mechanochromisms via Strain-Dependent Cracks and Folds. *Nat. Commun.* **2016**, *7*, 11802.
(35) Chen, C.; Zhuang, Y.; Li, X.; Lin, F.; Peng, D.; Tu, D.; Xie, A.; Xie, R. J. Achieving Remote Stress and Temperature Dual-Modal Imaging by Double-Lanthanide-Activated Mechanoluminescent Materials. *Adv. Funct. Mater.* **2021**, *31*, 2101567.
(36) Kim, M.; Timilsina, S.; Jang, S.; Kim, J.; Park, S. A Mechanoluminescent ZnS:Cu/PDMS and Biocompatible Piezoelectric Silk Fibroin/PDMS Hybrid Sensor for Self-Powered Sensing and Artificial Intelligence Control. *Adv. Mater. Technol.* **2024**, *9*, 2400255.
(37) Hajra, S.; Panda, S.; Song, S.; Panigrahi, B. K.; Pakawanit, P.; Jeong, S.; Kim, H. Flexible Composite Material for Self-Powered Applications via Triboelectricity and Mechanoluminescence: PDMS/ZnS:Cu Composites. *Nano Energy* **2023**, *114*, 108668.
(38) Li, J.; Zhang, Z.; Luo, X.; Zhu, L.; Wang, Z. Triboelectric Leakage-Field-Induced Electroluminescence Based on ZnS:Cu. *ACS Appl. Mater. Interfaces* **2022**, *14*, 4775−4782.

https://doi.org/10.1021/acs.analchem.5c05546
Anal. Chem. 2026, 98, 2098−2107